Frontiers of Information Technology & Electronic Engineering
www.jzus.zju.edu.cn; engineering.cae.cn; www.springerlink.com
ISSN 2095-9184 (print); ISSN 2095-9230 (online)
E-mail: jzus@zju.edu.cn

Acoustic localization with multi-layer isogradient sound speed profile using TDOA and FDOA*

Dongzhou ZHAN[1], Sitian WANG[1], Shougui CAI[1], Huarong ZHENG[2], Wen XU[†‡2]
[1]*College of Information Science and Electronic Engineering, Zhejiang University, Hangzhou 310027, China*
[2]*Key Laboratory of Ocean Observation-Imaging Testbed of Zhejiang Province, Ocean College,*
Zhejiang University, Zhoushan 316021, China
[†]E-mail: wxu@zju.edu.cn

Received Aug. 22, 2021; Revision accepted Nov. 1, 2021; Crosschecked Dec. 12, 2022

Abstract: In the underwater medium, the speed of sound varies with water depth, temperature, and salinity. The inhomogeneity of water leads to bending of sound rays, making the existing localization algorithms based on straight-line propagation less precise. To realize high-precision node positioning in underwater acoustic sensor networks (UASNs), a multi-layer isogradient sound speed profile (SSP) model is developed using the linear segmentation approximation approach. Then, the sound ray tracking problem is converted into a polynomial root-searching problem. Based on the derived gradient of the signal's Doppler shift at the sensor node, a novel underwater node localization algorithm is proposed using both the time difference of arrival (TDOA) and frequency difference of arrival (FDOA). Simulations are implemented to illustrate the effectiveness of the proposed algorithm. Compared with the traditional straight-line propagation method, the proposed algorithm can effectively handle the sound ray bending phenomenon. Estimation accuracy with different SSP modeling errors is also investigated. Overall, accurate and reliable node localization can be achieved.

Key words: Underwater acoustic sensor network; Acoustic localization; Sound speed profile; Time difference of arrival (TDOA); Frequency difference of arrival (FDOA)
https://doi.org/10.1631/FITEE.2100398 **CLC number:** TN98

1 Introduction

The emergence of underwater acoustic sensor networks (UASNs) has greatly improved the efficiency of marine environmental monitoring (Kong et al., 2005). In most UASN applications, precise node localization is fundamental and important. The node location information is the key to accomplishing other underwater tasks (Pompili and Akyildiz, 2009; Fan et al., 2011). In location-dependent data acquisition tasks, the data is useful only when the location information is correct (Ferguson et al., 2005; Li et al., 2018). Because the speed of sound underwater varies with water depth, salinity, and temperature, acoustic localization methods based on the assumption of straight-line sound propagation have inherent biases. More accurate localization algorithms with realistic sound speed profiles (SSPs) need to be developed.

Various methods have been proposed to solve the underwater localization problem. Basically, these methods can be divided into two major classes, range-free and range-based methods (Erol-Kantarci et al., 2011; Han et al., 2012). Range-free methods localize the target node according to the connectivity and topology of UASN without the range and bearing information (Chen et al., 2018). The accuracy of the range-free localization methods is not

---

[‡] Corresponding author

[*] Project supported by the National Key Research and Development Program of China (No. 2017YFC0305900) and the Zhejiang University K. P. Chao's High Technology Development Foundation (No. 2020ZL013)

ORCID: Dongzhou ZHAN, https://orcid.org/0000-0002-3119-2178

high and is limited by the number of sensor nodes. Range-based localization methods include time of arrival (TOA) (Luo et al., 2018), time difference of arrival (TDOA) (Liang et al., 2013), angle of arrival (AOA) (Huang and Zheng, 2018), frequency difference of arrival (FDOA) (Zhang et al., 2018), and received signal strength indicator (RSSI) (Sun et al., 2019). These methods first estimate the ranges or angles between the target node and the sensor nodes. Trilateration, triangulation, or multilateration methods are then used to localize the target node. Beaudeau et al. (2015) proposed a new RSSI-based multi-target tracking approach, and demonstrated the effectiveness of the approach in tracking a relatively large number of targets. However, the RSSI method performs terribly for long-range localization in an underwater environment. Huang and Zheng (2018) proposed a new multi-hop localization algorithm with AOA, which outperforms the conventional algorithms, even if the AOA measurement error is large.

However, accurate time synchronization is required between the sensors and the target, remaining a challenging task in UASNs. Although the TOA-based methods are simple to implement, a time synchronization problem exists. For unsynchronized UASNs, TDOA and FDOA are used commonly, especially for localization of moving sources (Ho et al., 2007; Tan et al., 2011).

All the range-based methods that use the straight-line propagation model ignore the sound-ray bending phenomenon. To mitigate the influence of the varying sound speed on localization, different sound models have been proposed. The effective sound velocity (ESV) model (Vincent and Hu, 1997) was proposed to compensate for the error caused by the bending of sound ray. However, ESV works well only in the deep-sea environment. Ameer and Jacob (2010) proposed that when the target depth is known, the TOA between the target node and each sensor node can be transformed into a constant range surfaces using an SSP. The position of the target is then derived as the point whose sum of the squared distances from all these surfaces is minimum. Although this method has a high localization accuracy, the main drawback is the significant computational complexity. In the case of the isogradient SSP, Ramezani et al. (2013) used geometric relationships to establish path equations among the nodes. The computational complexity is acceptable, because it is analytic. However, this method cannot be applied to more complex SSP scenarios.

In most applications of underwater localization using the TDOA and FDOA methods, the localization problem is nonlinear (Ho and Xu, 2004; Jiang et al., 2020). Therefore, various nonlinear methods have been proposed to localize the target node. Some of them are implemented iteratively based on maximum likelihood methods (Vankayalapati et al., 2014), such as the Gauss–Newton algorithm (GNA) (Doğançay and Hashemi-Sakhtsari, 2005). Ho et al. (2007) introduced closed-form solutions that require low computation capability. Linearization methods can be implemented in localization. Ho and Xu (2004) employed several weighted least-square minimizations to transform the nonlinear problem into a linear one. Furthermore, closed-form solutions of the nonlinear measurement equations were constructed step by step in Jia et al. (2019). However, considering the multi-layer isogradient SSP, the scenario we discuss in this paper is relatively complicated, and cannot be solved using linear methods or easily transformed into a linear one.

In this study, we first propose an analytical multi-layer isogradient SSP model for the sound ray path between nodes. We then propose a method to calculate the gradient of the frequency shift of the arrival signals. On this basis, we propose an FDOA-based node localization algorithm, and a location and velocity joint estimation algorithm based on TDOA and FDOA. The proposed algorithm tracks the sound ray effectively. Results from the simulations prove the effectiveness of the proposed algorithms. More accurate and reliable node localization can be attained, compared with the straight-line propagation method.

2 Multi-layer isogradient sound speed profile model and sound ray tracking

In this section, the mathematical multi-layer isogradient SSP model is described in detail.

As shown in Fig. 1, the green line represents the true SSP, and the red line represents the multi-layer isogradient SSP. The multi-layer model segments the true SSP into multiple layers with a piecewise linear function of water depth. Each layer has a constant gradient. There are a total of P segmented lines to approximate the true SSP (Fig. 1). Then, the sound speed $c_p(z)$ in the p^{th} sound ray layer can be expressed as

$$c_p(z) = a_p z + b_p,\ z \in [z_{p-1}, z_p), \tag{1}$$

where z is the water depth ranging from z_{p-1} to z_p, a_p is the gradient, and b_p is the horizontal-axis intercept. Both a_p and b_p are determined by the true SSP. As the number of layers becomes larger, the difference between the true SSP and the multi-layer SSP decreases.

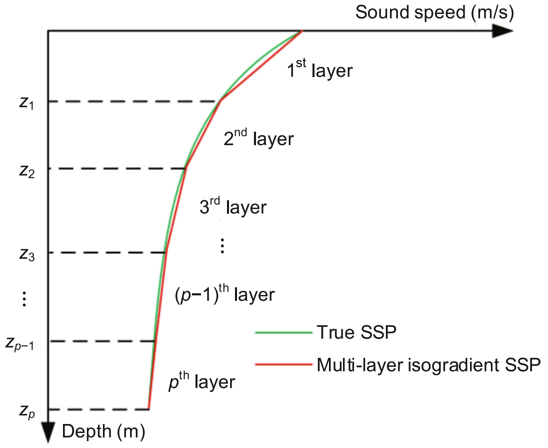

Fig. 1 A true sound speed profile (SSP) and a multi-layer isogradient SSP (References to color refer to the online version of this figure)

According to Snell's law (Shirley, 1951) and the geometric relationship of the sound ray, the starting point $\boldsymbol{S}_p = (x_p^{\text{S}}, y_p^{\text{S}}, z_p^{\text{S}})^{\text{T}}$ and the ending point $\boldsymbol{E}_p = (x_p^{\text{E}}, y_p^{\text{E}}, z_p^{\text{E}})^{\text{T}}$ in a single layer are related as (Cai, 2019)

$$d_p = \sqrt{\left(x_p^{\text{E}} - x_p^{\text{S}}\right)^2 + \left(y_p^{\text{E}} - y_p^{\text{S}}\right)^2}, \tag{2}$$

$$L_p = \frac{0.5a_p(z_p^{\text{E}} - z_p^{\text{S}})}{b_p + 0.5a_p(z_p^{\text{E}} + z_p^{\text{S}})}, \tag{3}$$

$$\begin{cases} X_p = (z_p^{\text{E}} - z_p^{\text{S}})/d_p, & (4) \\ Y_p = L_p/X_p, \quad \text{when } z_p^{\text{E}} \neq z_p^{\text{S}}, & (5) \end{cases}$$

$$\begin{cases} \alpha_p = \arctan Y_p, & (6) \\ \beta_p = \arctan X_p, & (7) \end{cases}$$

$$\begin{cases} \theta_p^{\text{S}} = \beta_p + \alpha_p, & (8) \\ \theta_p^{\text{E}} = \beta_p - \alpha_p, & (9) \end{cases}$$

$$t_p = \frac{-1}{a_p}\left[\ln\left(\frac{1+\sin\theta_p^{\text{E}}}{\cos\theta_p^{\text{E}}}\right) - \ln\left(\frac{1+\sin\theta_p^{\text{S}}}{\cos\theta_p^{\text{S}}}\right)\right], \tag{10}$$

where d_p is the horizontal distance between the starting and ending points of the sound ray, L_p is a constant determined by the characteristics of SSP, X_p and Y_p are the defined auxiliary variables, α_p is the angle between the actual acoustic ray path and the straight-line path, β_p is the angle between the straight-line path and the horizontal direction, and θ_p^{S} and θ_p^{E} are the glancing angles at the starting and ending points of the sound ray, respectively. The angles α_p, β_p, θ_p^{S}, and θ_p^{E} are illustrated directly in Fig. 2. The description of linetype is the same as in Fig. 1. The traveling time from $\boldsymbol{S}_p$ to $\boldsymbol{E}_p$ is denoted as t_p.

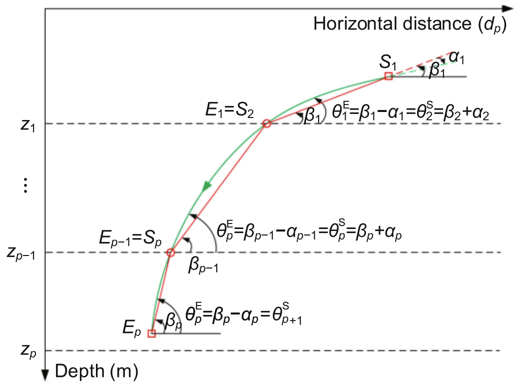

Fig. 2 Glancing angles of $\boldsymbol{\theta_p^{\text{E}}}$ and $\boldsymbol{\theta_{p+1}^{\text{S}}}$ (References to color refer to the online version of this figure)

Regardless of the reflection of the seabed and sea surface (Fig. 2), the glancing angles at the ending point of the p^{th} layer and the starting point of the $(p+1)^{\text{th}}$ layer are related as

$$\theta_p^{\text{E}} = \theta_{p+1}^{\text{S}},\ p = 1, 2, ..., P-1. \tag{11}$$

Using Eqs. (3)–(11) and the properties of trigonometric functions, we can obtain

$$\frac{X_{\text{p}+1} + \frac{L_{p+1}}{X_{p+1}}}{1 - L_{p+1}} = \frac{X_p - \frac{L_p}{X_p}}{1 + L_p}. \tag{12}$$

Eq. (12) is a high-order polynomial of X_p (or d_p). The calculated value of X_p is substituted into Eqs. (5)–(9) to find the θ_p^{S} and θ_p^{E} of each layer, thereby realizing sound ray tracking. Therefore, with the multi-layer model, the sound ray tracking is equivalent to determining the roots of the $p-1$ polynomials.

3 Moving target node localization

This section introduces two algorithms in detail, i.e., the FDOA localization algorithm and the joint estimation algorithm based on the TDOA (Cai, 2019), and FDOA for localization and velocity estimation of a moving target node. To fulfill either of the two algorithms, we need to know the gradient of certain spatial positions first.

3.1 Frequency gradient calculation

Assume that the velocities of the target and sensor nodes are not zero, and define the target position as $\boldsymbol{x}=[x,y,z]^{\mathrm{T}}$, the target velocity at position $\boldsymbol{x}$ as $\boldsymbol{v}_x=[v_x,v_y,v_z]^{\mathrm{T}}$, the sensor position as $\boldsymbol{a}=[x^a,y^a,z^a]^{\mathrm{T}}$, and the sensor velocity as $\boldsymbol{v}_a=[v_x^a,v_y^a,v_z^a]^{\mathrm{T}}$. With the multi-layer isogradient SSP model, the analytical expression of the frequency of arrival (FOA) from the transmitter to the receiver is

$$f=f_1-f_{\mathrm{D}}, \tag{13}$$

where f_1 is the shifted signal frequency related to the movement of the transmitter and f_{D} is the Doppler frequency shift produced by the movement of the receiver (Bogushevich, 1999):

$$f_1=f_0\frac{c_{\mathrm{s}}}{c_{\mathrm{s}}-v_{\perp\mathrm{s}}}, \tag{14}$$

$$f_{\mathrm{D}}=f_1\frac{v_{\perp\mathrm{r}}}{c_{\mathrm{r}}}, \tag{15}$$

where f_0 is the carrier frequency, c_{s} and c_{r} are the speed of sound at the depths of the target and sensor nodes, respectively, and $v_{\perp\mathrm{s}}$ and $v_{\perp\mathrm{r}}$ are the radial velocities of the target and sensor nodes, respectively. Moreover, $v_{\perp\mathrm{s}}$ and $v_{\perp\mathrm{r}}$ are given by

$$\begin{cases} v_{\perp\mathrm{s}}=(v_{\mathrm{s}x}\cos\varphi+v_{\mathrm{s}y}\sin\varphi)\cos\theta_1^{\mathrm{S}}+v_{\mathrm{s}z}\sin\theta_1^{\mathrm{S}}, & (16)\\ v_{\perp\mathrm{r}}=(v_{\mathrm{r}x}\cos\varphi+v_{\mathrm{r}y}\sin\varphi)\cos\theta_P^{\mathrm{E}}+v_{\mathrm{r}z}\sin\theta_P^{\mathrm{E}}. & (17)\end{cases}$$

Denote AT' as the line that connects the target's projection T' and sensor A. φ is the angle between AT' and the x-axis, and $\boldsymbol{v}_{\mathrm{s}}=[v_{\mathrm{s}x},v_{\mathrm{s}y},v_{\mathrm{s}z}]^{\mathrm{T}}$ and $\boldsymbol{v}_{\mathrm{r}}=[v_{\mathrm{r}x},v_{\mathrm{r}y},v_{\mathrm{r}z}]^{\mathrm{T}}$ are the velocity of the transmitter and receiver nodes, respectively (Fig. 3).

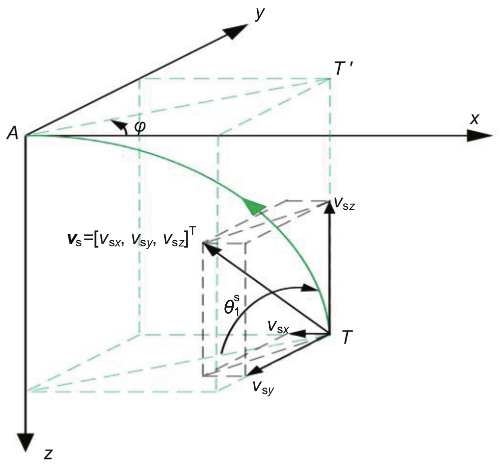

Fig. 3 Decomposition of speed $\boldsymbol{v}_{\mathrm{s}}$

When the target is the transmitter, the partial derivative of FOA to the target position can be obtained from Eq. (13) as

$$\frac{\partial f}{\partial x}=\frac{\partial f_1}{\partial x}-\frac{\partial f_{\mathrm{D}}}{\partial x}, \tag{18}$$

$$\frac{\partial f_1}{\partial x}=\frac{\partial f_1}{\partial\theta_1^{\mathrm{S}}}\frac{\partial\theta_1^{\mathrm{S}}}{\partial x}+\frac{\partial f_1}{\partial\varphi}\frac{\partial\varphi}{\partial x}, \tag{19}$$

$$\frac{\partial f_{\mathrm{D}}}{\partial x}=\frac{\partial f_{\mathrm{D}}}{\partial\theta_P^{\mathrm{E}}}\frac{\partial\theta_P^{\mathrm{E}}}{\partial x}+\frac{\partial f_{\mathrm{D}}}{\partial\varphi}\frac{\partial\varphi}{\partial x}, \tag{20}$$

where the partial derivatives are

$$\frac{\partial f_1}{\partial\theta_1^{\mathrm{S}}}=\frac{f_0c_{\mathrm{s}}}{(c_{\mathrm{s}}-v_{\perp\mathrm{s}})^2}\left(-v_h\sin\theta_1^{\mathrm{S}}+v_z\cos\theta_1^{\mathrm{S}}\right), \tag{21}$$

$$\frac{\partial f_1}{\partial\varphi}=\frac{f_0c_{\mathrm{s}}}{(c_{\mathrm{s}}-v_{\perp\mathrm{s}})^2}\left(-v_x\sin\varphi+v_y\cos\varphi\right)\cos\theta_1^{\mathrm{S}}, \tag{22}$$

$$\frac{\partial f_{\mathrm{D}}}{\partial\theta_P^{\mathrm{E}}}=\frac{f_1}{c_{\mathrm{r}}}\left(-v_h^{\mathrm{a}}\sin\theta_P^{\mathrm{E}}+v_z^{\mathrm{a}}\cos\theta_P^{\mathrm{E}}\right), \tag{23}$$

$$\frac{\partial f_{\mathrm{D}}}{\partial\varphi}=\frac{f_1}{c_{\mathrm{r}}}\left(-v_x^{\mathrm{a}}\sin\varphi+v_y^{\mathrm{a}}\cos\varphi\right)\cos\theta_P^{\mathrm{E}}, \tag{24}$$

where $v_h=v_x\cos\varphi+v_y\sin\varphi$, and $v_h^{\mathrm{a}}=v_x^{\mathrm{a}}\cos\varphi+v_y^{\mathrm{a}}\sin\varphi$ (a refers to the sensor node related parameters). Similarly, the partial derivatives of f with respect to the target's y- and z-axis coordinates can be obtained.

The partial derivative of FOA to the target velocity can also be obtained from Eq. (13) as

$$\frac{\partial f}{\partial v_x}=\left(1-\frac{v_{\perp\mathrm{r}}}{c_{\mathrm{r}}}\right)\frac{f_0c_{\mathrm{s}}}{(c_{\mathrm{s}}-v_{\perp\mathrm{s}})^2}\cos\varphi\cos\theta_P^{\mathrm{E}}. \tag{25}$$

Similarly, the partial derivatives of f with respect to the target's velocity components of the y- and z-axis can be obtained.

3.2 Frequency difference of the arrival localization algorithm

Consider a three-dimensional UASN with N sensor nodes. The positions and velocities of all the sensor nodes are known based on the global positioning system (GPS). Meanwhile, the velocity of the target node is assumed to be known for the FDOA localization algorithm for four sensor nodes. Recall that the position of the target node is $\boldsymbol{x}$; FOAs of the positioning signals received by the sensor node can then be modeled as

$$\boldsymbol{f}_f=\boldsymbol{g}(\boldsymbol{x})+\boldsymbol{n}, \tag{26}$$

where the actual signal arrival frequency $\boldsymbol{g}(\cdot)=[g_1(\cdot),g_2(\cdot),...,g_N(\cdot)]^{\mathrm{T}}$ is a function of the target position $\boldsymbol{x}$=$[x,y,z]^{\mathrm{T}}$ represented by Eq. (13), $\boldsymbol{f}_f=[f_{f_1},f_{f_2},...,f_{f_N}]^{\mathrm{T}}$ is the measured FOAs between the target and the individual sensors, and N-dimensional column vector $\boldsymbol{n}$ is the measurement noise, obeying the Gaussian distribution with a mean value of zero and a variance of $\boldsymbol{\Sigma}=\left[\sigma_{f_1}^2,\sigma_{f_2}^2,...,\sigma_{f_N}^2\right]^{\mathrm{T}}$. The corresponding measurement noises of individual sensor nodes are independent of each other.

Taking the first sensor node as the reference node, and subtracting the arrival frequencies of the reference node from the arrival frequencies of the other $N-1$ nodes, the FDOA measurement model is

$$\Delta\boldsymbol{f}=\boldsymbol{g}'(\boldsymbol{x})+\boldsymbol{\zeta}, \tag{27}$$

where $\Delta\boldsymbol{f}=[\Delta f_{21},\Delta f_{31},...,\Delta f_{N1}]^{\mathrm{T}}$, $\boldsymbol{g}'(\cdot)=[{g_{21}}'(\cdot),{g_{31}}'(\cdot),...,{g_{N1}}'(\cdot)]^{\mathrm{T}}$, $\boldsymbol{\zeta}=[\zeta_{21},\zeta_{31},...,\zeta_{N1}]^{\mathrm{T}}$, and

$$\Delta f_{i1}=f_{f_i}-f_{f_1}, \tag{28}$$

$${g_{i1}}'(\cdot)=g_i(\cdot)-g_1(\cdot), \tag{29}$$

$$\zeta_{i1}\sim\mathcal{N}(0,\sigma_{f_{i1}}^2), \tag{30}$$

$$\sigma_{f_{i1}}^2=\sigma_{f_i}^2+\sigma_{f_1}^2, i=2,3,...,N. \tag{31}$$

The covariance matrix of the noise vector can be obtained from Eq. (31) as

$$\boldsymbol{R}_{f\xi}=\sigma_{f_1}^2\boldsymbol{1}_{N-1}+\mathrm{diag}(\sigma_{f_2}^2,\sigma_{f_3}^2,...,\sigma_{f_N}^2), \tag{32}$$

where $\mathrm{diag}(\sigma_{f_2}^2,\sigma_{f_3}^2,...,\sigma_{f_N}^2)$ stands for a diagonal matrix, whose diagonal values are $\sigma_{f_2}^2,\sigma_{f_3}^2,...,\sigma_{f_N}^2$.

Because it is assumed that the measurement noise is Gaussian, the maximum likelihood estimate of target position $\boldsymbol{x}$ can be derived as

$$\hat{\boldsymbol{x}}=\arg\min_{\boldsymbol{x}}\left\{\left(\boldsymbol{g}'(\boldsymbol{x})-\Delta\boldsymbol{f}\right)^{\mathrm{T}}\boldsymbol{R}_{f\xi}^{-1}\left(\boldsymbol{g}'(\boldsymbol{x})-\Delta\boldsymbol{f}\right)\right\}. \tag{33}$$

Obviously, the solution represented by Eq. (33) is nonlinear, and GNA (Cai, 2019) can be used to find the solution. The GNA method uses Taylor series approximation to minimize Eq. (33), through multiple iterations. The k^{th} iteration can be expressed as

$$\boldsymbol{x}^{(k+1)}=\boldsymbol{x}^{(k)}-\left(\boldsymbol{J}_f{}^{\mathrm{T}}\boldsymbol{R}_{f\xi}^{-1}\boldsymbol{J}_f\right)^{-1}\boldsymbol{J}_f{}^{\mathrm{T}}\boldsymbol{R}_{f\xi}^{-1}\boldsymbol{r}_f, \tag{34}$$

where $\boldsymbol{J}_f=\nabla\boldsymbol{g}'(\boldsymbol{x}^{(k)})$, $\boldsymbol{r}_f=\boldsymbol{g}'(\boldsymbol{x}^{(k)})-\Delta\boldsymbol{f}$, and

$$\nabla\boldsymbol{g}'(\boldsymbol{x}^{(k)})=\left[\frac{\partial {g_2}'}{\partial\boldsymbol{x}},\frac{\partial {g_3}'}{\partial\boldsymbol{x}},...,\frac{\partial {g_N}'}{\partial\boldsymbol{x}}\right]_{\boldsymbol{x}=\boldsymbol{x}^{(k)}}^{\mathrm{T}}, \tag{35}$$

$$\frac{\partial {g_i}'}{\partial\boldsymbol{x}}=\frac{\partial g_i}{\partial\boldsymbol{x}}-\frac{\partial g_1}{\partial\boldsymbol{x}},\ i=2,3,...,N. \tag{36}$$

According to Eq. (18) and the solution methods proposed by Cai (2019), it can be obtained that $\frac{\partial g_i}{\partial\boldsymbol{x}}=\left[\frac{\partial g_i}{\partial x},\frac{\partial g_i}{\partial y},\frac{\partial g_i}{\partial z}\right]^{\mathrm{T}}(i=2,3,...,N)$. The pseudocode of this algorithm is listed in Algorithm 1.

Algorithm 1 GNA-based FDOA localization

```
Input: $\Delta\boldsymbol{f}$, FDOA; $\boldsymbol{R}_{f\xi}$, covariance matrix of the noise vector
Output: target position estimate $\hat{\boldsymbol{x}}=[\hat{x},\hat{y},\hat{z}]^{\mathrm{T}}$
set the initial value $\boldsymbol{x}_0$
set the maximum number of iterations $K$ and the iteration error limit $\varepsilon$
set the iteration number $k=1$, and assign a large value to iteration error $E$
while $k\leq K$ and $E\geq\varepsilon$ do
    $\boldsymbol{x}^{(k+1)}=\boldsymbol{x}^{(k)}-\left(\boldsymbol{J}_f{}^{\mathrm{T}}\boldsymbol{R}_{f\xi}^{-1}\boldsymbol{J}_f\right)^{-1}\boldsymbol{J}_f{}^{\mathrm{T}}\boldsymbol{R}_{f\xi}^{-1}\boldsymbol{r}_f$
    $E=\left\|\boldsymbol{x}^{(k+1)}-\boldsymbol{x}^{(k)}\right\|$
    $k=k+1$
end while
Return $\hat{\boldsymbol{x}}=\boldsymbol{x}^{(k)}$
```

Note that the target velocity is assumed to be known in the scenario of four sensor nodes for the FDOA localization algorithm. This assumption is actually not necessary if more (at least seven) sensor nodes are available, because both position and velocity information can be estimated from FDOAs. In other words, the considered four-sensor-node scenario cannot provide velocity information. Instead of using more sensor nodes, we propose a joint FDOA and TDOA method to estimate both the position and velocity information in the following subsections.

3.3 Joint estimation using both TDOA and FDOA

When the TDOA and FDOA measurements are combined to estimate the position and velocity of the moving target, the estimation can be achieved by increasing the dimension of the matrices mentioned above. The variable to be estimated is $\boldsymbol{\Phi}=[x,y,z,v_x,v_y,v_z]^{\mathrm{T}}$, and GNA is again used to solve the problem. First, the TOAs of the positioning signals received by the sensor node can be modeled as

$$\boldsymbol{t}=\boldsymbol{h}(\boldsymbol{\Phi})+\boldsymbol{n}_t, \tag{37}$$

where the actual signal arrival time $\boldsymbol{h}(\cdot)=[h_1(\cdot),h_2(\cdot),...,h_N(\cdot)]^{\mathrm{T}}$ is a function of $\boldsymbol{\Phi}$, $\boldsymbol{t}=[t_1,t_2,...,t_N]^{\mathrm{T}}$ is the measured TOAs between the target and the individual sensors, and N-dimensional column vector $\boldsymbol{n}_t$ is the measurement noise, obeying the Gaussian distribution with a mean value of zero and a variance of $\boldsymbol{\Sigma}_t=\left[\sigma_{t_1}^2,\sigma_{t_2}^2,...,\sigma_{t_N}^2\right]^{\mathrm{T}}$. The corresponding measurement noises of individual sensor nodes are independent of each other. Each item of $\boldsymbol{h}(\cdot)$ can be described in detail as

$$h_i(\cdot)=\sum_{p=1}^{P}\frac{-1}{a_p}\left[\ln\left(\frac{1+\sin\theta_p^{\mathrm{E}}}{\cos\theta_p^{\mathrm{E}}}\right)-\ln\left(\frac{1+\sin\theta_p^{\mathrm{S}}}{\cos\theta_p^{\mathrm{S}}}\right)\right], \tag{38}$$

where P is the number of the total layers through which the sound ray travels.

Taking the first sensor node as the reference node, and subtracting the arrival times of the reference node from other $N-1$ nodes, the TDOA measurement model is

$$\Delta\boldsymbol{t}=\boldsymbol{h}'(\boldsymbol{\Phi})+\boldsymbol{\rho}, \tag{39}$$

where $\Delta\boldsymbol{t}=[\Delta t_{21},\Delta t_{31},...,\Delta t_{N1}]^{\mathrm{T}}$, $\boldsymbol{h}'(\cdot)=[h_{21}{}'(\cdot),h_{31}{}'(\cdot),...,h_{N1}{}'(\cdot)]^{\mathrm{T}}$, $\boldsymbol{\rho}=[\rho_{21},\rho_{31},...,\rho_{N1}]^{\mathrm{T}}$, and

$$\Delta t_{i1}=t_i-t_1, \tag{40}$$

$$h_{i1}{}'(\cdot)=h_i(\cdot)-h_1(\cdot), \tag{41}$$

$$\rho_{i1}\sim\mathcal{N}(0,\sigma_{t_{i1}}^2), \tag{42}$$

$$\sigma_{t_{i1}}^2=\sigma_{t_i}^2+\sigma_{t_1}^2, i=2,3,...,N. \tag{43}$$

The covariance matrix of the noise vector can be obtained from Eq. (43) as

$$\boldsymbol{R}_{t\xi}=\sigma_{t_1}^2\boldsymbol{1}_{N-1}+\mathrm{diag}(\sigma_{t_2}^2,\sigma_{t_3}^2,...,\sigma_{t_N}^2). \tag{44}$$

Following the same procedure as mentioned in the FDOA localization algorithm, the maximum likelihood estimate of $\boldsymbol{\Phi}$ can be derived as

$$\hat{\boldsymbol{\Phi}}=\arg\min_{\boldsymbol{\Phi}}\left\{\boldsymbol{r}^{\mathrm{T}}\boldsymbol{R}_{\xi}^{-1}\boldsymbol{r}\right\}, \tag{45}$$

and the k^{th} iteration of the GNA method can be expressed as

$$\boldsymbol{\Phi}^{(k+1)}=\boldsymbol{\Phi}^{(k)}-\left(\boldsymbol{J}^{\mathrm{T}}\boldsymbol{R}_{\xi}{}^{-1}\boldsymbol{J}\right)^{-1}\boldsymbol{J}^{\mathrm{T}}\boldsymbol{R}_{\xi}{}^{-1}\boldsymbol{r}, \tag{46}$$

where

$$\boldsymbol{J}=\begin{pmatrix}\nabla\boldsymbol{g}'(\boldsymbol{\Phi}^{(k)})\\ \nabla\boldsymbol{h}'(\boldsymbol{\Phi}^{(k)})\end{pmatrix}, \tag{47}$$

$$\boldsymbol{R}_{\xi}=\begin{pmatrix}\boldsymbol{R}_{f\xi} & \boldsymbol{0}\\ \boldsymbol{0} & \boldsymbol{R}_{t\xi}\end{pmatrix}, \tag{48}$$

$$\boldsymbol{r}=\begin{pmatrix}\boldsymbol{g}'(\boldsymbol{\Phi}^{(k)})\\ \boldsymbol{h}'(\boldsymbol{\Phi}^{(k)})\end{pmatrix}-\begin{pmatrix}\Delta\boldsymbol{f}\\ \Delta\boldsymbol{t}\end{pmatrix}. \tag{49}$$

$\nabla\boldsymbol{h}'(\boldsymbol{\Phi}^{(k)})$ can be expressed as

$$\nabla\boldsymbol{h}'(\boldsymbol{\Phi}^{(k)})=\left[\frac{\partial h_2{}'}{\partial\boldsymbol{\Phi}},\frac{\partial h_3{}'}{\partial\boldsymbol{\Phi}},...,\frac{\partial h_N{}'}{\partial\boldsymbol{\Phi}}\right]^{\mathrm{T}}_{\boldsymbol{\Phi}=\boldsymbol{\Phi}^{(k)}}, \tag{50}$$

and

$$\frac{\partial h_i{}'}{\partial\boldsymbol{\Phi}}=\frac{\partial h_i}{\partial\boldsymbol{\Phi}}-\frac{\partial h_1}{\partial\boldsymbol{\Phi}}, i=2,3,...,N. \tag{51}$$

According to Eq. (38), h_i is irrelevant to $[v_x,v_y,v_z]^{\mathrm{T}}$, and thus

$$\frac{\partial h_i}{\partial\boldsymbol{\Phi}}=\left[\frac{\partial h_i}{\partial x},\frac{\partial h_i}{\partial y},\frac{\partial h_i}{\partial z},0,0,0\right]^{\mathrm{T}}. \tag{52}$$

It is obvious that the analytical expressions of $\nabla\boldsymbol{h}'(\boldsymbol{\Phi}^{(k)})$, $\boldsymbol{R}_{t\xi}$, $\boldsymbol{h}'(\boldsymbol{\Phi}^{(k)})$, and $\Delta\boldsymbol{t}$ are similar to those of $\nabla\boldsymbol{g}'(\boldsymbol{\Phi}^{(k)})$, $\boldsymbol{R}_{f\xi}$, $\boldsymbol{g}'(\boldsymbol{\Phi}^{(k)})$, and $\Delta\boldsymbol{f}$. The GNA-based joint estimation algorithm is shown in Algorithm 2.

For TDOA, FDOA, and joint estimation algorithms, the localization results might not be unique (Cheng et al., 2008). The reason is that all the three algorithms are based on triangulation. It is difficult for triangulation to have a unique and global optimal solution. In most cases, it is possible to tell which result is correct using physical constraints. To overcome the uniqueness and optimality issues, extra sensor nodes could be introduced, for example, using five sensor nodes instead of four in the case of the FDOA algorithm.

4 Simulations and discussions

This section presents two sets of simulations. The first set verifies the localization performance of the proposed joint estimation algorithm. Two error surfaces of position and velocity estimation are given.

Algorithm 2 GNA-based joint estimation

```
Input: $\Delta\boldsymbol{f}$, FDOA; $\Delta\boldsymbol{t}$, TDOA; $\boldsymbol{R}_\xi$, covariance matrix of the noise vector
Output: target position and velocity estimation $\hat{\boldsymbol{\Phi}} = [\hat{x}, \hat{y}, \hat{z}, \hat{v}_x, \hat{v}_y, \hat{v}_z]^{\mathrm{T}}$
set the initial value $\boldsymbol{\Phi}_0$
set the maximum number $K$ of iterations and the iteration error limit $\varepsilon$
set the iteration number $k = 1$, and assign a large value to the iteration error $E$
while $k \le K$ and $E \ge \varepsilon$ do
    $\boldsymbol{\Phi}^{(k+1)} = \boldsymbol{\Phi}^{(k)} - \left(\boldsymbol{J}^{\mathrm{T}}\boldsymbol{R}_\xi{}^{-1}\boldsymbol{J}\right)^{-1}\boldsymbol{J}^{\mathrm{T}}\boldsymbol{R}_\xi{}^{-1}\boldsymbol{r}$
    $E = \left\|\boldsymbol{\Phi}^{(k+1)} - \boldsymbol{\Phi}^{(k)}\right\|$
    $k = k + 1$
end while
Return $\hat{\boldsymbol{\Phi}} = \boldsymbol{\Phi}^{(k)}$
```

Root-mean-square errors (RMSEs) were used to evaluate the accuracy of the proposed joint estimation algorithm. The second set compares the position and velocity RMSEs of the three algorithms, i.e., FDOA, TDOA (Cai, 2019), and joint estimation, separately. All simulations were performed with both the multi-layer isogradient SSP and straight-line propagation models.

4.1 Descriptions of the simulation environment

The configuration of the sensor nodes is shown in Table 1. In the simulations, four sensors were set up in a parallelogram topology with the same side length of 2 km. The target was set at the depth of 800 m. The sensor nodes were located at the depth of 10.2 m from the sea surface. The true velocity of the target node was $\boldsymbol{v}_x = [-2.0, 1.5, 4.0]^{\mathrm{T}}$ m/s. All signals were transmitted from the target node to the sensor nodes. The true SSP used in the simulations is shown in Fig. 4. The sound speed at the sea surface was 1500 m/s, and the sound speed at the depth of 1000 m was 1490 m/s. This SSP is expressed as

$$c(z) = 1500 - (z/10)^{1/2}. \tag{53}$$

Table 1 Positions and velocities of the sensor nodes

Sensor	Position (m)			Velocity (m/s)		
index i	x_i	y_i	z_i	v_{xi}	v_{yi}	v_{zi}
1	0	0	10.2	0.3	−2.0	0.2
2	2000	0	10.2	−1.0	0.1	0.5
3	1000	1732.05	10.2	0.9	−0.3	1.0
4	3000	1732.05	10.2	1.0	2.0	0.6

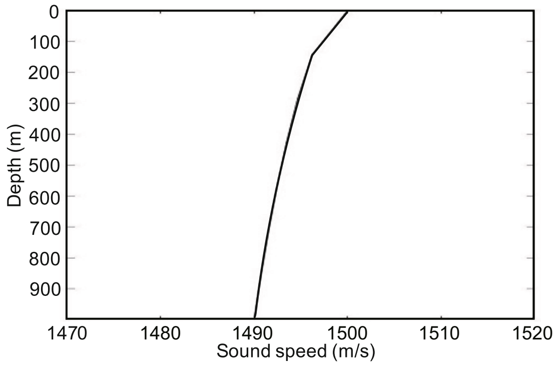

Fig. 4 True sound speed profile

Then the true SSP was divided into nine even layers. The gradient of each layer can be described as

$$a_p = \frac{c_p(z_{\mathrm{s}}) - c_p(z_{\mathrm{d}})}{D_{\mathrm{L}}}, \tag{54}$$

where $c_p(z_{\mathrm{s}})$ and $c_p(z_{\mathrm{d}})$ are the sound speeds at the shallowest and deepest depths of the p^{th} layer, respectively, and D_{L} is the thickness of the layer. The sensor nodes were assumed to be synchronized, while the time it took for sound to travel between the target and the sensor nodes was not synchronized. The carrier frequency of the signals sent by the target to the sensors was 1000 Hz.

For the GNA-based algorithms, K and ε, which control the number of iterations, were set as $K = 20$ and $\varepsilon = 1$.

4.2 Verification of the proposed joint estimation algorithm

This subsection verifies the accuracy of the proposed joint estimation algorithm using RMSE. RMSE was used to measure the differences between $\hat{\boldsymbol{x}}^{(k)}$ predicted by a model or an estimator and the true value $\boldsymbol{x}^{(k)}$. By observing K times, RMSE can be obtained by

$$\mathrm{RMSE} = \left(\frac{1}{K}\sum_{k=1}^{K}\left(\hat{\boldsymbol{x}}^{(k)} - \boldsymbol{x}^{(k)}\right)^2\right)^{1/2}. \tag{55}$$

All the TDOA and FDOA measurements in the following simulations were generated by adding noise to true values, which were generated through the multi-layer isogradient SSP model. In sea trials, the TDOA and FDOA values can be estimated from the received signals using the ambiguity function (Zhan et al., 2014), which can be expressed as

$$\mathrm{AF}(\tau, f)=\int_{-\infty}^{\infty} s_{\mathrm{r}}(t) s_1^*(t-\tau) \exp(\mathrm{j} 2\pi f t) \mathrm{d}t, \quad (56)$$

where $\mathrm{AF}(\tau, f)$ stands for the ambiguity function, $s_{\mathrm{r}}(t)$ is the complex baseband form of the received signal that contains noise, $s_1(t)$ is the reference signal, $*$ denotes the complex conjugate, and j is the imaginary unit. When $\mathrm{AF}(\tau, f)$ reaches its peak with $\tau=\tau_0$ and $f=f_0$, τ_0 and f_0 are the TDOA and FDOA, respectively.

In Figs. 5 and 6, the standard deviation of the time-delay measurement noise was $\sigma_t^2=1\times10^{-8}$ s^2, and the standard deviation of the frequency measurement noise was $\sigma_f^2=1\times10^{-9}$ Hz^2. These two noises were independent. The estimation error surfaces were given by the statistical average of 1000 Monte Carlo simulations, and the length of the grid was 100 m.

Figs. 5 and 6 show the estimation error surfaces of the position and velocity in the area enclosed by the four sensor nodes, respectively. The straight-line propagation model and multi-layer model localization accuracies are illustrated in the same graph. From the estimation error surfaces in Figs. 5 and 6, we can see that the error was the largest at the two acute angles of the parallelogram. The closer to the center point of the parallelogram, the smaller the error value was. In both position and velocity estimation error graphs, the straight-line propagation model error was at least 20 dB larger than that of the multi-layer model.

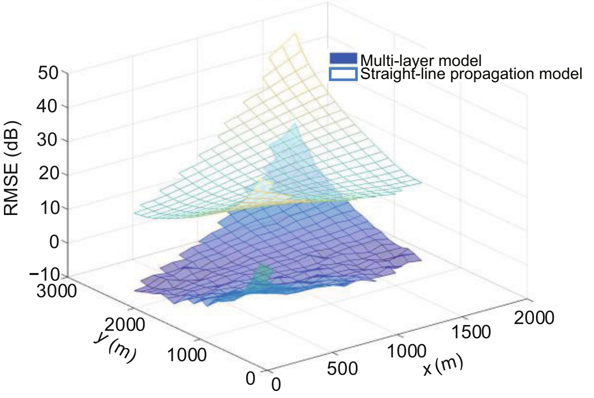

Fig. 5 Positioning error surfaces of the two models

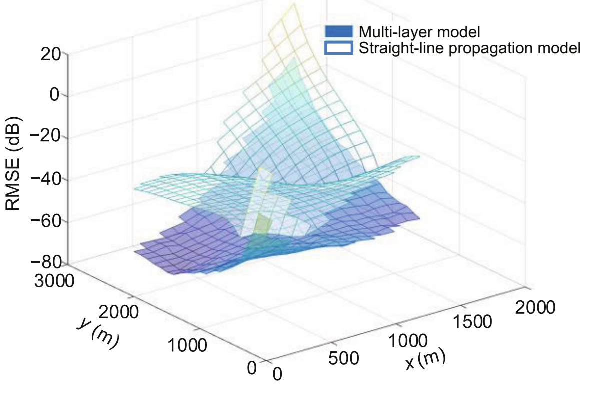

Fig. 6 Velocity error surfaces of the two models

Fig. 7 illustrates the convergence of the location estimation using the GNA-based FDOA localization algorithm. The true position of the target node was $[1000, 800, 800]^{\mathrm{T}}$ m. The initial position value $[1006, 815, 775]^{\mathrm{T}}$ m was calculated using the straight-line propagation model. The × mark was used to represent the initial position of the GNA iteration, and the star mark was used to represent the true value. The entire convergence process was enlarged for easy viewing. It can be seen that after two iterations, the position estimation was close to the true position along with the iteration path of GNA. In fact, the convergence tended to be fast throughout the localization process. This is because the initial values derived from the straight-line propagation model were close to the true position values. Moreover, GNA had a good convergence property and always converged quickly. It often took only a few iterations to converge to a value that was close to the true value with the GNA-based FDOA localization algorithm.

We used RMSE to test the performance of the three algorithms with the multi-layer model, including the individual localization performance of the TDOA and FDOA algorithms and the joint

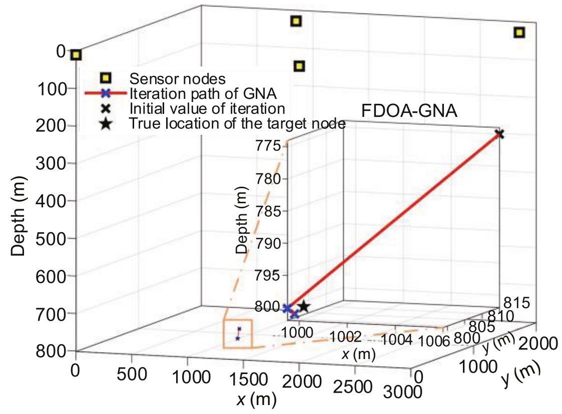

Fig. 7 Convergence of the location estimation using the Gauss–Newton algorithm (GNA) based frequency difference of arrival (FDOA) localization algorithm

estimation algorithm. The results are shown in Figs. 8 and 9. The time delay measurement noise is an important factor that affects the algorithm accuracy. In the simulations, the time delay measurement noise ranged from 1×10^{-8} s^2 to 1×10^{-4} s^2. The frequency measurement noise was set to be 1/10 of the time delay measurement noise, and ranged from 1×10^{-9} Hz^2 to 1×10^{-5} Hz^2. The time delay measurement noise was not related to the Doppler shift measurement noise. The start position of the target was $\boldsymbol{x}=[1000, 800, 800]^{\mathrm{T}}$ m. Error curves were given by the statistical average of 10 000 Monte Carlo simulations. From the simulation results (Figs. 8 and 9), we can see that as the measurement accuracy increased, while other conditions remained unchanged, the algorithm error decreased.

As can be seen from the TDOA positioning results (Fig. 8), when there was little measurement noise, the performance of the straight-line propagation model was significantly inferior to that of the multi-layer model. When there was significant measurement noise, the accuracies of the two models were almost the same, because by then, the main factor affecting the position accuracy was the measurement noise instead of the modeling error. The results of the FDOA positioning in Fig. 8 showed that when there was little measurement noise, the error of the straight-line propagation model was caused mainly by the inaccurate glancing angle of the sound ray. The effect of the measurement error was relatively small, and the performance of the straight-line propagation model was obviously inferior to that of the

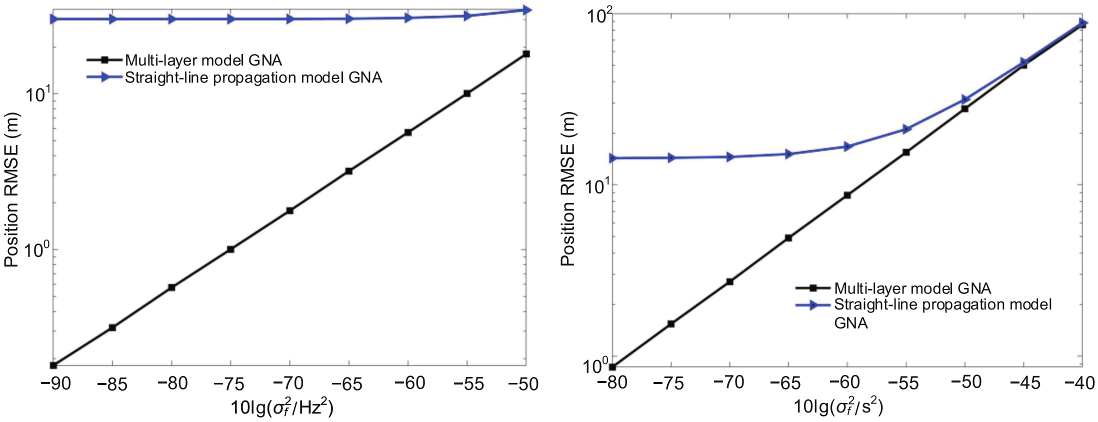

(a) (b)

Fig. 8 Positioning errors of the FDOA (a) and TDOA (b) algorithms (RMSE: root-mean-square error; GNA: Gauss–Newton algorithm)

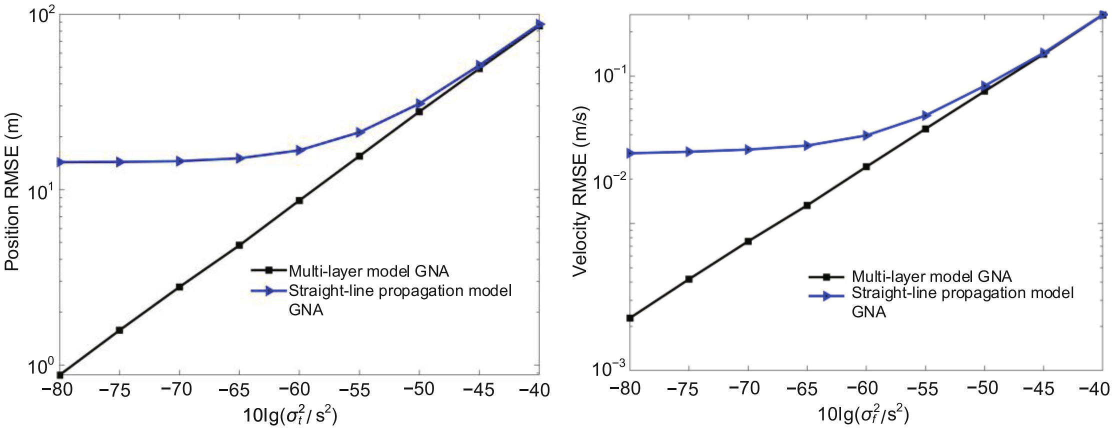

(a) (b)

Fig. 9 Positioning (a) and velocity (b) errors of the joint estimation algorithm (RMSE: root-mean-square error; GNA: Gauss–Newton algorithm)

multi-layer model. When the measurement noise was significant enough, the accuracies of the two models tended to be the same.

It is obvious from the results of the joint estimation (Fig. 9) that as the measurement noise increased, the position accuracy decreased. In this case, the position accuracy tended to be influenced by the measurement accuracy instead of the modeling accuracy.

However, by comparing the results in Figs. 8 and 9, we can see that the multi-layer model can more accurately and reliably determine the target node position and estimate velocity in underwater scenarios with curved sound rays. Because the overall gradient of the selected SSP in the simulations was quite small, the influence of the modeling error on the estimation results was also small, especially when the measurement noise was significant.

4.3 Comparison with different sound speed profile layers

Simulation results in Figs. 10 and 11 showed the estimation accuracy under different SSP modeling errors. In addition to the nine-layer SSP model described above, evenly segmented two- and five-layer models were introduced to represent different modeling errors. It is clear that with more layers, the proposed multi-layer SSP was closer to the true SSP. Therefore, the modeling errors of the two- and five-

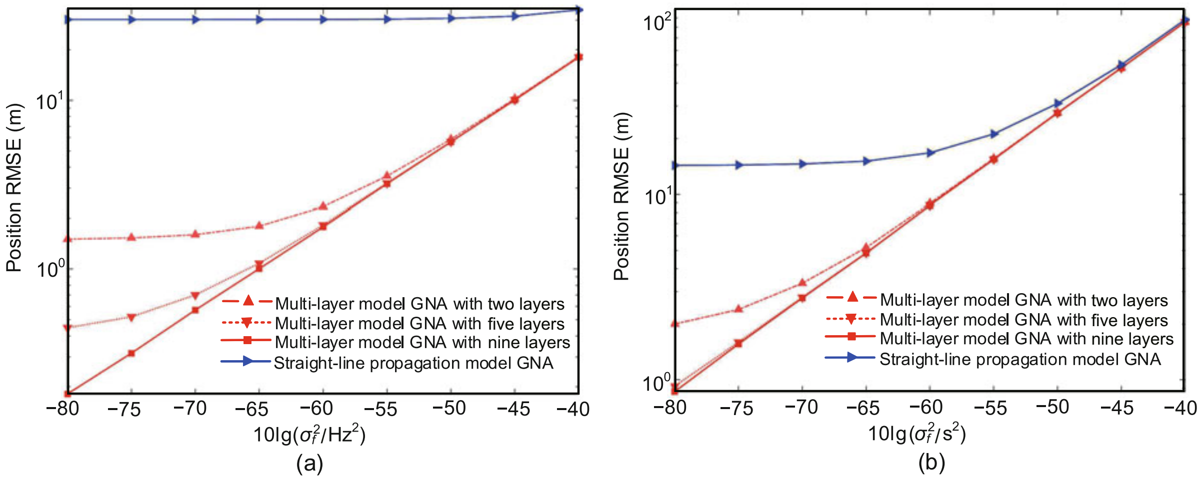

Fig. 10 Positioning errors of the FDOA (a) and TDOA (b) algorithms with two, five, and nine layers (RMSE: root-mean-square error; GNA: Gauss–Newton algorithm)

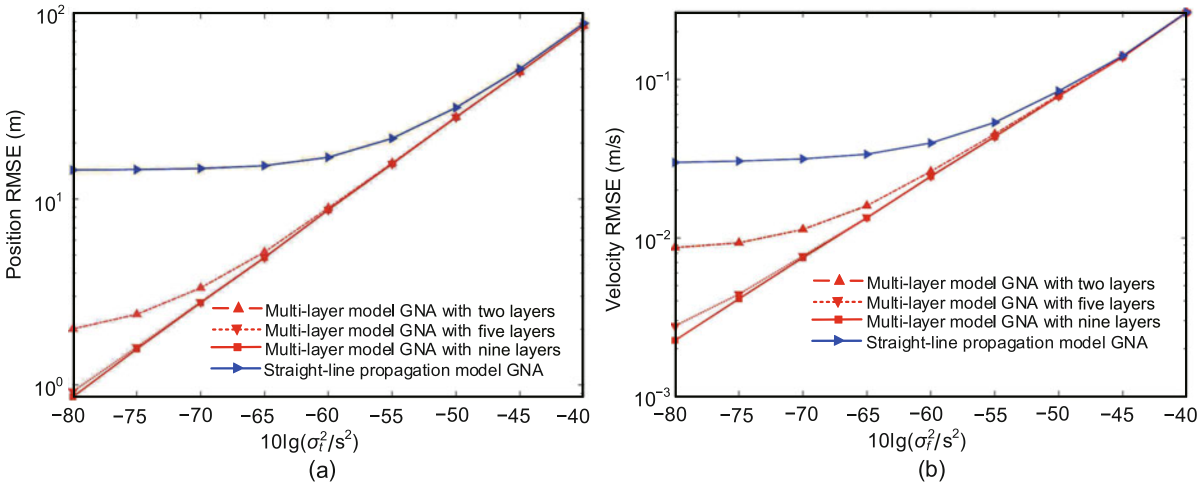

Fig. 11 Positioning (a) and velocity (b) errors of the joint estimation algorithm with two, five, and nine layers (RMSE: root-mean-square error; GNA: Gauss–Newton algorithm)

layer models were greater than those of the nine-layer model. With the same simulation settings as mentioned in Section 4.2, all the curves in Figs. 10 and 11 were given by the statistical average of 10 000 Monte Carlo simulations. The results (Figs. 10 and 11) showed that smaller modeling errors led to higher estimation accuracy, for both velocity and position estimations. Therefore, the nine-layer model had the highest estimation accuracy in all the cases, and the two-layer model was the worst.

Overall, simulation results showed that localization algorithms based on the multi-layer model can effectively track the sound ray, correct the estimation error caused by sound ray bending, and give a more reliable and accurate node position and velocity estimation, compared with the traditional straight-line propagation model. Higher SSP modeling accuracy led to higher localization and velocity accuracy.

5 Conclusions

The curvature of sound ray in the underwater medium has a non-negligible effect on localization performance. Aiming to mitigate this effect, we discuss the moving target localization and velocity estimation methods. The algorithms proposed are based on the multi-layer isogradient SSP. Through the segmentation of SSP, the analytical expression of SSP is established. On this basis, we propose the gradient calculation method of the Doppler shift between the target and the sensor nodes to improve target localization. Based on GNA, we solve the problem of target node localization. Simulation results show that the algorithms based on the multi-layer model can effectively track the sound ray and mitigate the errors created by the single-layer straight-line SSP, thus giving more reliable and accurate estimations of the position and velocity of the moving target.

Contributors

Wen XU conceptualized this paper, administrated the whole project, and raised the funding acquisition. Huarong ZHENG and Wen XU supervised the research. Dongzhou ZHAN, Sitian WANG, and Shougui CAI proposed the methodology. Sitian WANG developed the software, and Huarong ZHENG validated it. Sitian WANG visualized the results. Dongzhou ZHAN and Sitian WANG drafted the paper. Huarong ZHENG and Wen XU revised and finalized the paper.

Compliance with ethics guidelines

Dongzhou ZHAN, Sitian WANG, Shougui CAI, Huarong ZHENG, and Wen XU declare that they have no conflict of interest.

Data availability

The data that support the findings of this study are available from the corresponding author upon reasonable request.

References

Ameer PM, Jacob L, 2010. Localization using ray tracing for underwater acoustic sensor networks. *IEEE Commun Lett*, 14(10):930-932. https://doi.org/10.1109/LCOMM.2010.090810.101237

Beaudeau JP, Bugallo MF, Djurić PM, 2015. RSSI-based multi-target tracking by cooperative agents using fusion of cross-target information. *IEEE Trans Signal Processing*, 63(19):5033-5044. https://doi.org/10.1109/TSP.2015.2448530

Bogushevich AY, 1999. To an analysis of the acoustic Doppler effect in a three-dimensional inhomogeneous moving medium. *Atmos Ocean Opt*, 12(4):301-308.

Cai SJ, 2019. Research on Positioning Error Correction in Underwater Acoustic Sensor Network with Sound Speed Inversion. MS Thesis, Zhejiang University, Hangzhou, China (in Chinese).

Chen HY, Liu MQ, Zhang SL, 2018. Energy-efficient localization and target tracking via underwater mobile sensor networks. *Front Inform Technol Electron Eng*, 19(8):999-1012. https://doi.org/10.1631/FITEE.1700598

Cheng XZ, Shu HN, Liang QL, et al., 2008. Silent positioning in underwater acoustic sensor networks. *IEEE Trans Veh Technol*, 57(3):1756-1766. https://doi.org/10.1109/TVT.2007.912142

Doğançay K, Hashemi-Sakhtsari A, 2005. Target tracking by time difference of arrival using recursive smoothing. *Signal Processing*, 85(4):667-679. https://doi.org/10.1016/j.sigpro.2004.11.007

Erol-Kantarci M, Mouftah HT, Oktug S, 2011. A survey of architectures and localization techniques for underwater acoustic sensor networks. *IEEE Commun Surv Tutor*, 13(3):487-502. https://doi.org/10.1109/SURV.2011.020211.00035

Fan GY, Chen HF, Xie L, et al., 2011. Funneling media access control (MAC) protocol for underwater acoustic sensor networks. *J Zhejiang Univ Sci C (Comput & Electron)*, 12(11):932-941. https://doi.org/10.1631/JZUS.C1000388

Ferguson BG, Lo KW, Thuraisingham RA, 2005. Sensor position estimation and source ranging in a shallow water environment. *IEEE J Ocean Eng*, 30(2):327-337. https://doi.org/10.1109/JOE.2004.838064

Han GJ, Jiang JF, Shu L, et al., 2012. Localization algorithms of underwater wireless sensor networks: a survey. *Sensors*, 12(2):2026-2061. https://doi.org/10.3390/s120202026

Ho KC, Xu WW, 2004. An accurate algebraic solution for moving source location using TDOA and FDOA measurements. *IEEE Trans Signal Processing*, 52(9):2453-2463. https://doi.org/10.1109/TSP.2004.831921

Ho KC, Lu XN, Kovavisaruch L, 2007. Source localization using TDOA and FDOA measurements in the presence of receiver location errors: analysis and solution. *IEEE Trans Signal Processing*, 55(2):684-696. https://doi.org/10.1109/TSP.2006.885744

Huang H, Zheng YR, 2018. Node localization with AoA assistance in multi-hop underwater sensor networks. *Ad Hoc Netw*, 78:32-41. https://doi.org/10.1016/j.adhoc.2018.05.005

Jia TY, Ho KC, Wang HY, et al., 2019. Effect of sensor motion on time delay and Doppler shift localization: analysis and solution. *IEEE Trans Signal Processing*, 67(22):5881-5895. https://doi.org/10.1109/TSP.2019.2946025

Jiang F, Zhang ZK, Najafabadi HE, et al., 2020. Underwater TDOA/FDOA joint localisation method based on cross-ambiguity function. *IET Radar Sonar Navig*, 14(8):1256-1266. https://doi.org/10.1049/iet-rsn.2020.0003

Kong JJ, Cui JH, Wu DP, et al., 2005. Building underwater ad-hoc networks and sensor networks for large scale real-time aquatic applications. Processing IEEE Military Communications Conf, p.1535-1541. https://doi.org/10.1109/milcom.2005.1605894

Li B, Xu YX, Fan SS, et al., 2018. Underwater docking of an under-actuated autonomous underwater vehicle: system design and control implementation. *Front Inform Technol Electron Eng*, 19(8):1024-1041. https://doi.org/10.1631/FITEE.1700382

Liang QL, Zhang BJ, Zhao CL, et al., 2013. TDoA for passive localization: underwater versus terrestrial environment. *IEEE Trans Parall Distrib Syst*, 24(10):2100-2108. https://doi.org/10.1109/TPDS.2012.310

Luo JL, Han Y, Fan LY, 2018. Underwater acoustic target tracking: a review. *Sensors*, 18(1):112. https://doi.org/10.3390/s18010112

Pompili D, Akyildiz IF, 2009. Overview of networking protocols for underwater wireless communications. *IEEE Commun Mag*, 47(1):97-102. https://doi.org/10.1109/MCOM.2009.4752684

Ramezani H, Jamali-Rad H, Leus G, 2013. Target localization and tracking for an isogradient sound speed profile. *IEEE Trans Signal Processing*, 61(6):1434-1446. https://doi.org/10.1109/TSP.2012.2235432

Shirley JW, 1951. An early experimental determination of Snell's law. *Am J Phys*, 19(9):507-508. https://doi.org/10.1119/1.1933068

Sun YL, Yuan YZ, Xu QM, et al., 2019. A mobile anchor node assisted RSSI localization scheme in underwater wireless sensor networks. *Sensors*, 19(20):4369. https://doi.org/10.3390/s19204369

Tan HP, Diamant R, Seah WKG, 2011. A survey of techniques and challenges in underwater localization. *Ocean Eng*, 38(14-15):1663-1676. https://doi.org/10.1016/j.oceaneng.2011.07.017

Vankayalapati N, Kay S, Ding Q, 2014. TDOA based direct positioning maximum likelihood estimator and the Cramer-Rao bound. *IEEE Trans Aerosp Electron Syst*, 50(3):1616-1635. https://doi.org/10.1109/TAES.2013.110499

Vincent H, Hu SLJ, 1997. Geodetic position estimation of underwater acoustic sensors. *J Acoust Soc Am*, 102(5):3099-3100. https://doi.org/10.1121/1.420498

Zhan DZ, Zhao HF, Xu W, 2014. Non-linear processing based on dolphin inspired real LFM signals for enhanced delay-Doppler resolution. OCEANS, p.1-7. https://doi.org/10.1109/oceans-taipei.2014.6964562

Zhang BB, Hu YC, Wang HY, et al., 2018. Underwater source localization using TDOA and FDOA measurements with unknown propagation speed and sensor parameter errors. *IEEE Access*, 6:36645-36661. https://doi.org/10.1109/ACCESS.2018.2852636